

Identification of ferroelectric domain structure sensitive phonon modes in potassium titanyl phosphate: A fundamental study

M. Rüsing,^{a)} C. Eigner, P. Mackwitz, G. Berth, C. Silberhorn, and A. Zrenner
 Department Physik, Universität Paderborn, 33095 Paderborn, Germany

(Received 15 September 2015; accepted 18 January 2016; published online 28 January 2016)

Confocal Raman spectroscopy is applied to identify ferroelectric domain structure sensitive phonon modes in potassium titanyl phosphate. Therefore, polarization-dependent measurements in various scattering configurations have been performed to characterize the fundamental Raman spectra of the material. The obtained spectra are discussed qualitatively based on an internal mode assignment. In the main part of this work, we have characterized z-cut periodically poled potassium titanyl phosphate in terms of polarity- and structure-sensitive phonon modes. Here, we find vibrations whose intensities are linked to the ferroelectric domain walls. We interpret this in terms of changes in the polarizability originating from strain induced by domain boundaries and the inner field distribution. Hence, a direct and 3D visualization of ferroelectric domain structures becomes possible in potassium titanyl phosphate. © 2016 AIP Publishing LLC.

[<http://dx.doi.org/10.1063/1.4940964>]

I. INTRODUCTION

Potassium titanyl phosphate (KTP) is a ferroelectric material typically applied for optical frequency conversion processes. It has drawn particular attention due to its large electro-optical and non-linear coefficients.^{1–4} These properties are accompanied with a wide optical transparency window ranging from 0.35 μm to 4.3 μm ,⁵ a relatively small refractive index,² a low photo-refraction, and a high damage threshold compared with other commonly used materials in nonlinear optics, such as Lithium Niobate (LN).⁴ Moreover, KTP presents a prototype for a large material family with comparable properties.^{3,5} The combination of these properties makes KTP an ideal material for integrated nonlinear optics. A key requirement for achieving high conversion efficiencies in any nonlinear process is phase-matching between signal/idler and pump beams. Here, ferroelectric materials offer the possibility to employ the so-called quasi-phase-matching technique by periodic inversion of ferroelectric domains, which enables phase matching over a wide spectral range. A precondition for achieving high conversion efficiencies is high grade domain structures. In this context, a detailed characterization of the underlying formation mechanism is essential for fabrication process optimization. Several methods for the characterization of ferroelectric domain structures are known. One of the widest employed techniques is selective chemical etching. This technique makes use of the fact that the etching rate on the surface of ferroelectrics is sensitive to the ferroelectric domain orientation,^{6–8} which recently was explained in terms of different chemisorption energies on surfaces depending on the domain orientation.⁹ The obtained pattern then is observed by optical microscopy, electron microscopy, or scanning probe microscopy techniques.^{10,11} In KTP, only z-faces can be etched,¹² whereas in the common nonlinear materials LN and lithium

tantalate (LT) domains on z- and y-faces can be visualized by selective etching.¹³ Another standard method is Piezo-response Force Microscopy (PFM), a derivative of atomic force microscopy, which is directly sensitive to domain walls (DWs) and domain orientation. This method offers a high spatial resolution and is non-invasive.^{11,14} However, selective etching and PFM offer only information about the surface appearance of domains, whereas this can differ from the domain structure in depth.¹² Interior views of domain structures with both methods can only be obtained with high effort and at the cost of the non-invasive character.

On the contrary, optical methods offer the possibility for non-invasive three-dimensional imaging of ferroelectric domains inside crystals. Here, numerous properties and physical effects have been exploited in the past for *in-situ* and *ex-situ* visualization of ferroelectric domains, e.g., observation of phase shifts induced by the electro-optic effect in anti-parallel oriented domains,¹⁵ surface second harmonic (SH) generation,⁸ Čerenkov type SH generation,^{16,17} or utilizing group velocity mismatch of femto-second type II SHG pulses.¹⁸ In particular, confocal optical microscopy techniques offer 3D spatial resolution in the sub-micron regime and can be enhanced with contrast mechanisms sensitive to ferroelectric domain structures. Confocal optical microscopy does not require further treatment of samples and is non-invasive. Here, we can distinguish two main mechanisms, which are typically applied for the visualization of ferroelectric domains. One is SH microscopy, which makes use of the fact that the SH generation efficiency is sensitive to the crystal structure, which is perturbed in the vicinity of domain walls. Hence, detecting the spatially resolved SH intensity allows for direct visualization of domains.^{19–22} The second mechanism is Raman scattering, which is commonly used in the field of solid state systems. Here, the inelastic scattering gives access to numerous material properties.^{23,24} In the uniaxial ferroelectric materials LN and LT, it has been found that the intensity of certain phonon modes is connected to

^{a)}Electronic mail: michael.ruesing@upb.de

the ferroelectric domain structure. Here, a spatial mapping of these intensities allows for 3D visualization of both, domains and domain walls.^{10,11,25–27} Likewise, in the multi-axial material, barium titanate polarized confocal Raman spectroscopy has been successfully applied for a detailed three-dimensional analysis of domains and domain orientation.^{28–30}

SH microscopy as well as Raman spectroscopy enable a noninvasive analysis of domain structures. However, SH microscopy provides only limited further information on crystal structure or stoichiometric composition. On the contrary, Raman spectroscopy provides a deeper insight on the properties of ferroelectric crystals, e.g., electro-optic³¹ and dielectric properties^{32,33} or defects and stoichiometry.^{34,35}

In this paper, we apply confocal Raman spectroscopy to periodically poled KTP (PPKTP) in z-cut geometry to study and identify phonon modes sensitive to ferroelectric domains. Previously in KTP, it has been shown that SH microscopy can be applied for the visualization of ferroelectric domain structure. To our knowledge, it is yet to be shown that Raman modes can be used to visualize ferroelectric domains in KTP. For an interpretation of the behavior of phonon modes, which are sensitive to the domain structure, it is necessary to characterize the vibrational modes in a single domain bulk crystal. Usually, for confocal Raman imaging, a back scattering geometry is applied. Therefore, the first part of this work deals with the characterization of the occurring phonon modes obtained in all typical scattering configurations in the confocal setup in back-scattering geometry. In the second part, it is shown that ferroelectric domain structures can indeed be visualized by means of Raman imaging in KTP.

II. EXPERIMENTAL DETAILS

KTP is a member of a large material family with the formula $MTiOXO_4$, where M can be K, Rb, Tl, NH_4 , or Cs and X can be P, As, Si, or Ge.^{3,36} At room temperature, most members of the KTP family belong to the non-centrosymmetric point group $mm2$ (C_{2v}). Therefore, they show the pyroelectric and piezo-electric effect. The crystal structure can be approximated by chains of TiO_6 octahedrons, which are linked at two corners and are separated by PO_4 tetrahedrons.⁴ The potassium ion K^+ can be found at two different sites in between the web of octahedral and tetrahedral structures, coordinated by eight or nine oxygen atoms, respectively. A sketch of this structure in a x - z plane is shown in Fig. 1. The K^+ ions are only weakly bound to their sites and can easily migrate in channels along the z -axis as indicated by the dashed line. This explains the observed large ionic conductivity of the material in z -direction.³

The origin of the ferroelectricity is still part of an ongoing debate. The two main contributors to the polarization field, which are discussed, are alternating short and long Ti-O bonds³ and the displacement of potassium ions to alternative sites below the ferroelectric Curie temperature.^{36,37} In detail, four medium length Ti-O bonds in the range of 1.95 to 2.07 Å are reported. Along the z -axis, one short length bond of about 1.72–1.74 Å and a long bond of about 2.0–2.1 Å are observed.³

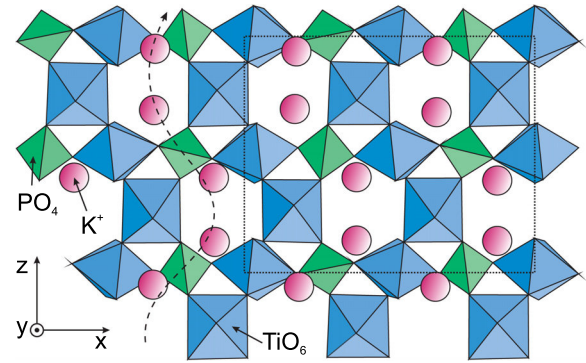


FIG. 1. Sketch (not true to scale) of the crystal structure in a x - z -plane viewed from the y -direction. The crystal is built up by chains of TiO_6 octahedrons (blue) proceeding along the z -axis. The octahedrons are linked at two corners and are separated by PO_4 tetrahedrons (green). The K^+ ion (red) is only weakly bound to its sites and can easily be moved in channels along the z -axis (dashed line). The dotted rectangular shows an area containing eight formula units and gives an estimate for the size of the unit cell.

The orthorhombic unit cell contains eight formula units resulting in up to 189 optical phonon modes! According to group theory, the vibrations can be further subdivided into different symmetry groups³⁸

$$\Gamma_{vib} = 47A_1(z) + 48A_2 + 47B_1(x) + 47B_2(y). \quad (1)$$

Here, the letter in brackets indicates the corresponding polarization of the phonons in crystal coordinates for the respective branch. All symmetry species are Raman active and nearly all are infrared (IR) active with the exception of A_2 modes. Hence, A_2 -phonons are non-polar and will not show a splitting of longitudinal optical (LO) and transverse optical (TO) modes at the Brillouin zone center. The Raman tensors for the orthorhombic point group C_{2v} are

$$A_1 = \begin{pmatrix} a & 0 & 0 \\ 0 & b & 0 \\ 0 & 0 & c \end{pmatrix}, \quad A_2 = \begin{pmatrix} 0 & d & 0 \\ d & 0 & 0 \\ 0 & 0 & 0 \end{pmatrix}, \quad (2)$$

$$B_1 = \begin{pmatrix} 0 & 0 & e \\ 0 & 0 & 0 \\ e & 0 & 0 \end{pmatrix}, \quad B_2 = \begin{pmatrix} 0 & 0 & 0 \\ 0 & 0 & f \\ 0 & f & 0 \end{pmatrix}.$$

The scattering geometries in this experiment are given in Porto's notation $k_i(e_i, e_s)k_s$, where the vector $k_{i,s}$ denotes the direction of the incident and scattered light in crystal coordinates, while $e_{i,s}$ references the polarization of the light. In a given scattering geometry, the observed intensity I can be calculated with the Raman tensor $R(x_n)$ and is given by

$$I \propto |e_s R(x_n) e_i|^2. \quad (3)$$

This study was performed on a confocal optical setup in back scattering geometry. The light of a frequency doubled Nd:YAG laser ($\lambda = 532$ nm, maximum output power of 50 mW) was focused via a long working distance objective lens onto the sample (Mitutoyo Plan Apo SL, 100 \times , $NA = 0.55$). In this study, a 10 μ m pinhole was used for confocal arrangement. For the confocal Raman imaging measurements, a scanning process is realized by a piezo-driven 3D-positioning

unit (Piezosystem Jena, Tritor) with respect to a fixed laser focus. The spectral analysis was performed via a single stage spectrometer with holographic grating and appropriate notch filter (KOSI Holospec f/1.8i) with an attached CCD camera (Andor Newton, BI) and a spectral resolution of about 2.3 cm^{-1} . Further details about the setup can be found in the previous publications.^{27,39}

In this work, three-dimensionally resolved confocal microscopy is performed in KTP, which is a highly biaxial birefringent material. Previous experimental and theoretical work on focused beams in an anisotropic medium has shown that the behavior of the focus inside the material can heavily deviate from the behavior in an isotropic medium, especially when focusing several millimeters below the surface of the anisotropic medium.^{40–42} In this work, we are mainly interested in a surface-near region of typically $<30 \mu\text{m}$, which, for example, is a typical diffusion depth of Rb-diffused waveguides. Therefore, we neglect any anisotropy effects for further discussion of the optical resolution. Due to the experimental geometry in this work, our incident and scattered light will be polarized along the x- and y-axes of the crystal. Hence, we assume a homogeneous medium with $n_x \approx n_y \approx 1.78$ for the refractive index at our laser wavelength.² The optical resolution can be characterized by the FWHM of the point spread function (PSF) of the objective lens. Here, the PSF is calculated via the software package *PSF lab*,⁴³ which can simulate a focused beam in a homogeneous refractive medium. In vacuum ($n = 1$), our optical system provides a spatial resolution (FWHM of the PSF) of $<2.9 \mu\text{m}$ in depth and $<530 \text{ nm}$ in lateral directions. When focused into a refractive medium, the PSF will be distorted due to refraction at the interface. In about $30 \mu\text{m}$, this leads to a decreased axial resolution of $<5.4 \mu\text{m}$, while lateral resolution is nearly unaffected ($<500 \text{ nm}$).

The samples have been fabricated in the in-house technology in Paderborn. Commercially available flux-grown KTP wafers (*Raicol Crystals Ltd.*) are cut to dimensions of $10 \times 6 \times 1 \text{ mm}^3$ (x-y-z directions) and afterwards polished in order to obtain high surface quality. The PPKTP sample was fabricated with a contact electrode technique.⁴⁴ A periodic metal grating is deposited on a glass substrate (period length of $\Lambda = 16.7 \mu\text{m}$ with a duty cycle $D = 10/6.7$, $10 \mu\text{m}$ electrode, and $6.7 \mu\text{m}$ gaps) and is pressed on the $-z$ -side of the KTP sample to act as a front electrode. The back-electrode is a planar gold-palladium layer directly deposited on the KTP sample. The domain inversion, which is operated at room temperature, is performed by applying several pulses of 2.5 kV generated with a high voltage pulse generator (*Trek 20/20c*). The progress is monitored via an optical method based on the transverse electro-optic effect to verify the successful poling.⁴⁵ The transferred domain structure is aligned parallel to the y-direction in crystal coordinates as shown in the inset in Fig. 3. The sample has not been chemically etched to ensure a clear 3D microscopic image.

III. RESULTS

A. Fundamental spectra

Based on Equation (3), the observed symmetry species and corresponding tensor elements have been calculated for

the complete set of back-scattering geometries, which is summarized in Table I. Due to back-scattering, only phonons propagating along main crystal axes will be excited. As the direction of lattice displacements for each symmetry species is given, we are further able to distinguish LO and TO modes. Here, TO modes can be observed for all symmetry species, while LO modes can only be detected for A_1 symmetry. Spectra have been recorded in a wavenumber range from 120 cm^{-1} to 1200 cm^{-1} . The lower limit is given by the transmission bandwidth of the notch filter. For a qualitative comparison, the spectra have been normalized to maximum after subtracting the dark count level (Fig. 2). As expected from group theory, a large number (>40) of phonons can be identified in every scattering geometry. Here, each symmetry species shows a characteristic spectral structure. Characteristic features of the A_1 -TO spectra are three high intensity bands^{46–48} at 209 cm^{-1} , 267 cm^{-1} , and 691 cm^{-1} , for example, while a characteristic signature of the A_1 -LO spectrum is an intense feature at 760 cm^{-1} . Apart from the characteristic features, the general shape of the spectra shows similarities in all symmetry species. The low wavenumber range $<200 \text{ cm}^{-1}$ only shows low intensity peaks. From 200 cm^{-1} to 350 cm^{-1} , each spectrum is dominated by a group of two to four medium to high intensity peaks, which carry a great portion of the overall scattered intensity. The 350 cm^{-1} to 690 cm^{-1} range is comprised a large number of low to medium intensity peaks. The most dominating feature for the Raman spectrum of KTP is one high intensity peak in the 690 cm^{-1} to 800 cm^{-1} range, which is the characteristic for the respective symmetry species. Further, a group of some low intensity peaks in the high wavenumber range (950 cm^{-1} to 1200 cm^{-1}) are a typical feature of the Raman spectrum of KTP.

All fundamental spectra have been recorded under the same conditions, which allows for a comparison of observed intensities in different spectra. Based on the integrated intensity over a complete spectrum, the tensor element squares have been estimated. For comparison, all integrated intensities have been normalized with respect to the spectrum with the lowest intensity, which belongs to the A_2 symmetry (d^2 element). The data is summarized in Table I and are in good agreement with the previous observations.³⁸ The

TABLE I. Raman selection rules for the complete set of back-scattering geometries given in Porto's notation and observed tensor elements calculated based on Equation (3). The last column gives a relative estimate for the tensor element squares deduced from the experiment. The observed intensities are normalized to d^2 -element from A_2 -symmetry.

Symmetry species	Scattering geometry	Tensor elements	Norm. intensity (experiment)
A_1 -LO	$z(x,x)\bar{z}$	a^2	1.8
A_1 -LO	$z(y,y)\bar{z}$	b^2	9.0
A_1 -TO	$y(x,x)\bar{y}$	a^2	4.2
A_1 -TO	$x(y,y)\bar{x}$	b^2	11.2
A_1 -TO	$x(z,z)\bar{x}$	c^2	26.3
A_2	$z(x,y)\bar{z}$	d^2	1.0
B_1 -TO	$y(x,z)\bar{x}$	e^2	1.9
B_2 -TO	$x(y,z)\bar{x}$	f^2	10.2

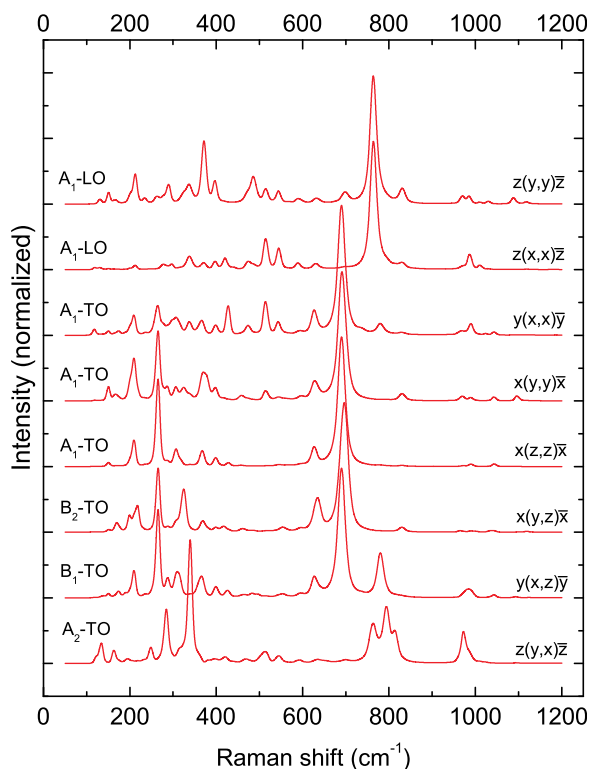


FIG. 2. Fundamental Raman spectra of KTP measured in the complete set of back-scattering geometries. On the left hand side, the spectra are labeled with the scattering geometry and on the right hand side the respective scattering geometry is given in Porto's notation (see Sec. II). For a qualitative comparison, the spectra are normalized (see text).

excitation and detection via an objective lens with a numerical aperture of $NA=0.55$ might lead to leakage effects due to a k -vector distribution in the focus.^{49,50} In particular, this effect may be partly responsible for some features in the A_1 -LO spectra, which are discussed in more detail below, such as peaks at 625 cm^{-1} or 693 cm^{-1} , which are close to the spectral position of very intense peaks in the A_1 -TO and B_2 -TO spectra.

B. Spectroscopic analysis of ferroelectric domains

From Raman studies in periodically poled LN and LT, it is known that the integrated intensities J of certain Raman bands are modified by the presence of DWs.^{10,11,25,27,51} For identifying phonon modes, which are sensitive to the domain structure, polarized Raman spectra in $z(y,y)\bar{z}$, $z(x,x)\bar{z}$ (A_1 -LO), and $z(y,x)\bar{z}$ (A_2) scattering geometries are recorded every 200 nm along a $65\text{ }\mu\text{m}$ line parallel to the x -axis. The measurement geometry and principle are shown in the inset in Fig. 3. Based on the identified peaks in the fundamental Raman spectra from Sec. III A, the integrated intensities J in the FWHM range are evaluated for each phonon. The obtained values are recorded with respect to their spatial coordinates and are analyzed for any periodic signal variations connected to the fabricated domain structure parameters. Here, we find a clear signature of the domain structure in the integrated intensities for numerous A_1 -LO phonons, as depicted in Fig. 3, while most phonons, as well as the Rayleigh scattered light (0 cm^{-1} Raman shift), do not show any correlation to the domain period, which rules out any

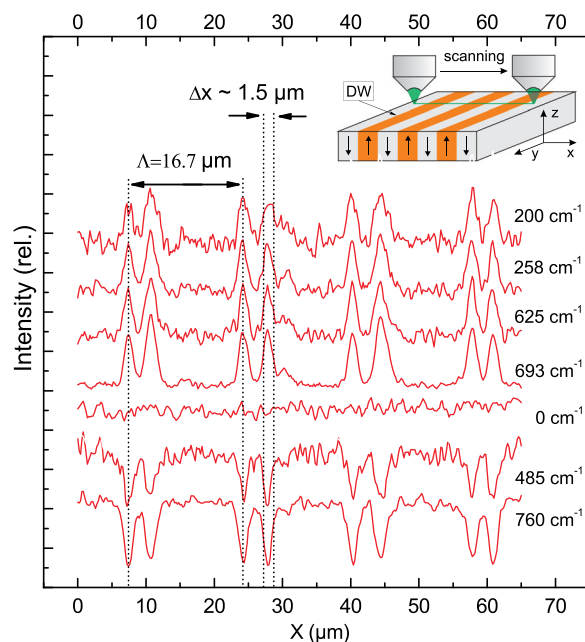


FIG. 3. Spatial variations of the integrated intensity J of selected Raman lines labeled by their peak frequency in $z(y,y)\bar{z}$. The sample geometry and scanning direction are shown in the inset. Signatures of domain walls are visible in the integrated intensity of several Raman lines, while the Rayleigh scattered light (0 cm^{-1}) shows no signature.

surface structure to be responsible for the signal. The observed signal variation appears to be solely connected to the DWs. So far, we could not detect any polarity contrast between domains of different signs, which has been observed in LN or LT.^{10,27} No major differences are found in the behavior of A_1 -LO phonons excited in $z(y,y)\bar{z}$ and $z(x,x)\bar{z}$ geometries. For A_2 phonons, no significant behavior connected to the domain is observed. Therefore, further analysis was limited to the $z(y,y)\bar{z}$ geometry. The observed period length of $\Lambda = (16.7 \pm 0.3)\text{ }\mu\text{m}$ agrees well with the fabrication parameter of the contact electrode. But the inverted ferroelectric domains show a significant broadening compared with the size of the contact electrodes ($10\text{ }\mu\text{m}$ of the contact electrode vs. $12\text{ }\mu\text{m}$ observed domain width in the samples). These observations agree well with the previous studies on the fabrication of periodically poled structures by contact poling in KTP, where a similar domain broadening was observed. This behavior was explained in terms of less nucleation sites compared to electrodes fabricated by photolithography techniques and less insulation of the air gaps in the contact electrodes.⁴⁴

For further analysis, two as-measured spectra taken on a DW [Fig. 4(a)] and in bulk are compared [Fig. 4(b)]. For clarity, the difference spectrum is included [Fig. 4(c)]. Overall, the spectra taken on a DW and in bulk are very similar. The main difference is found in the intensities of some peaks, which either increase or decrease at DWs, which is seen in the difference spectrum, while most phonon signatures appear unaffected. In the DW spectrum, no additional peaks are observed. A shift in the order of $\Delta\omega = 1\text{ cm}^{-1}$ of the intense feature at 760 cm^{-1} can only be resolved after fitting with a Lorentzian. This is visible in the asymmetry in the difference spectrum at 760 cm^{-1} (Fig. 4(c)), which reveals a shift

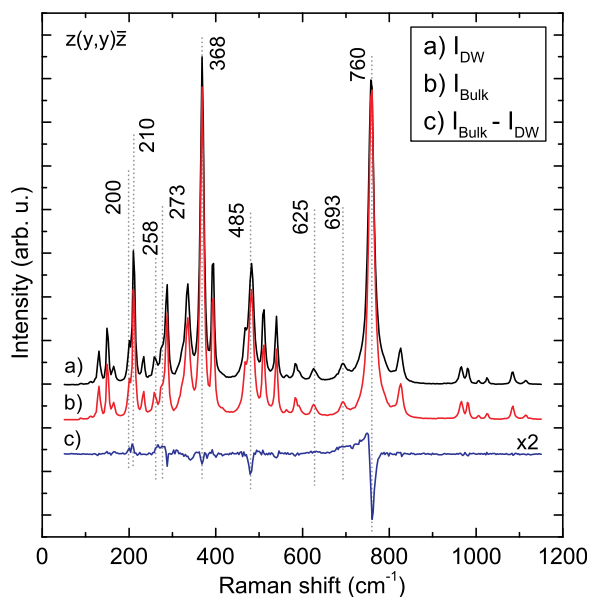


FIG. 4. Comparison of two as-measured Raman spectra taken on a DW (a) and in bulk (b). For clarity, the spectra are separated by an arbitrary offset and a difference spectrum is included (c).

to slightly lower frequencies in the DW spectrum. Further shifts are not observable but might be masked by spectral resolution. In LN and LT, for example, the reported differences in peak positions between bulk and DW Raman spectra are smaller than $<1 \text{ cm}^{-1}$ and have also been reported to recover to its bulk value after a period of time.^{10,25,26}

Best candidates for the visualization of domain structures are summarized in Table II. The table includes an estimation of the observed contrast defined as the relative enhancement of the integrated intensities between bulk and DW counts ($c = J_{DW}/J_{bulk} - 1$). Especially, the high intensity feature at 760 cm^{-1} and a small neighboring peak at 693 cm^{-1} allow for high-contrast imaging. Based on line scans in different depths starting at the surface, we do not find any change in the observed contrast behavior for the checked phonons, which hints at the absence of surface related effects.

C. Visualization of domains

Based on the described method, 2D images are obtained. Also, larger areas can be analyzed in a reasonable time. A

TABLE II. Contrast of selected A_1 -LO phonons in $z(y,y)\bar{z}$ geometry. The associated crystal component is given according to Refs. 38 and 46. The line at 625 cm^{-1} could not unambiguously be assigned.

Wavenumber in cm^{-1}	Contrast c^a (%)	Related crystal building block
150	5	K^+
200	6	TiO_6
258	13	K^+
273	13	K^+
485	-5	PO_4
625	13	$\text{TiO}_6?$
693	29	TiO_6
760	-7	TiO_6

^a $(c = J_{DW}/J_{bulk} - 1)$.

$65 \mu\text{m}$ (x) \times $20 \mu\text{m}$ (y) area was scanned with steps of $200 \text{ nm} \times 400 \text{ nm}$, respectively, and an integration time of 3 s per pixel. The resulting high contrast images based on the intensity of different phonons are displayed in Figs. 5(c)–5(f). For comparison, again the image based on the intensity of the Rayleigh scattered light [Fig. 5(a)] and a phonon with no correlation [Fig. 5(b)] are included. The images contain four poling periods and show y -aligned domains. At about $x = 15 \mu\text{m}$ and $x = 30 \mu\text{m}$, some residual domains are visible, which have not been inverted during poling. Here, the inversion may have been prohibited locally due to defects enhancing the coercive field. Fig. 6 shows a cross section of a domain structure along an xz -plane visualized with the integrated intensity of the 693 cm^{-1} mode. The image was obtained by taking line scans in different depths below the crystal surface. It should be noted that the measuring depth is corrected for focal shift due to refraction^{43,52} in a Gaussian beam formalism.^{53,54} The measurement shows that images of domain structures can easily be obtained for depth up to $30 \mu\text{m}$, which is, for example, sufficient to analyze ion-exchanged optical waveguides. Overall, images of domain structures can unambiguously and non-invasively be obtained with 3D Raman imaging and show the strength of this method.

IV. DISCUSSION

A. Fundamental spectra

Overall, the measured fundamental spectra agree well with the data reported in literature.^{38,46–48} For the interpretation of the behavior of certain phonon modes with respect to the domain structure it is helpful, if certain crystal structures can be assigned to certain spectral features. Due to the large number of phonons, no assignment of phonons to certain atom displacements patterns is available. A first approach to this issue is provided by an internal mode assignment. The main idea is to assign major features in the Raman spectra to internal modes of substructures of the KTP lattice, namely, the TiO_6 octahedron, the PO_4 tetrahedron, and the K^+ ion. We will only briefly discuss the results of an internal mode assignment, based on the analysis found in Refs. 38 and 46. The K^+ ion is only weakly bound to its site, which is the reason for the high ionic conductivity. Hence, only low frequency features are expected. A comparison of the Raman spectra to other members of the KTP family, e.g., TiTiOPO_4 and RbTiOPO_4 , reveals low intensity peaks mainly located in the region $<350 \text{ cm}^{-1}$ to be related to the K^+ ion.^{46,55} Further features in the low frequency region might be related to vibrations of complete substructures with respect to the lattice due to the low frequency character of such vibrations. Vibrations of the TiO_6 octahedron are found to be responsible for some of the most intensive features of the Raman spectrum in KTP. In detail, these are medium to high intensity features arising in the 200 to 350 cm^{-1} range and the most dominant peak arising at 690 cm^{-1} to 760 cm^{-1} in various geometries. Further, some low intensity features at 600 – 690 cm^{-1} and 830 – 840 cm^{-1} are expected to be related to internal modes of the TiO_6 . The PO_4 tetrahedron is nearly symmetric with average P-O bond length of 1.54 \AA in the

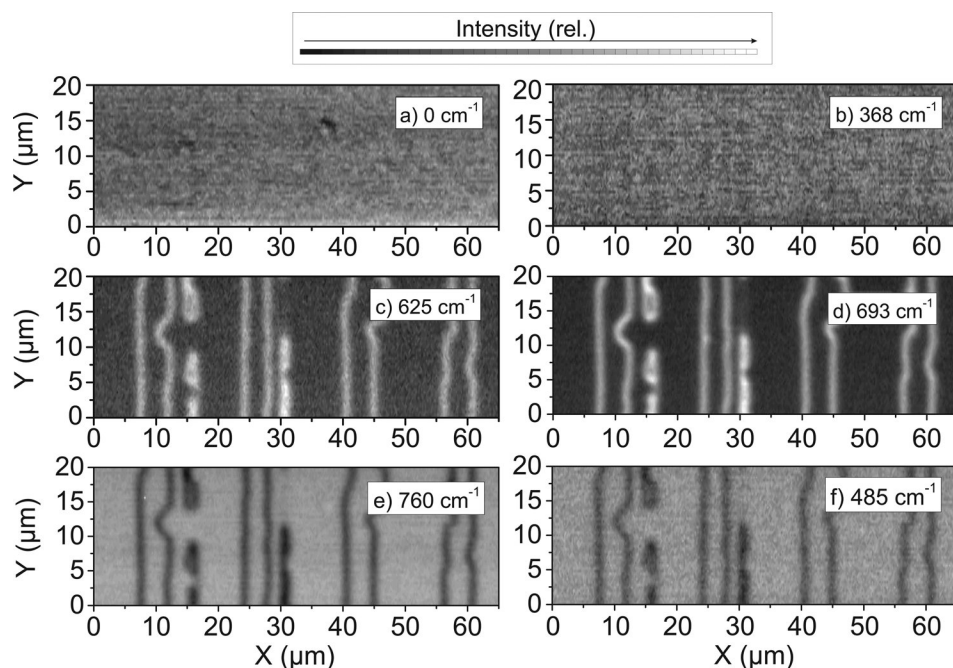


FIG. 5. High contrast 2D Raman images of domain structures. Some phonons offer positive contrast ((c) and (d)), other negative contrast ((e) and (f)). Picture (a) is an image generated based on the not shifted Rayleigh scattered light, while (b) is an example for an imaged based on a phonon with no significant connection to the domain structure.

KTP crystal.⁵⁶ According to Herzberg,⁵⁷ the four fundamental modes of a free PO_4 tetrahedron are expected to arise at 363 cm^{-1} , 515 cm^{-1} , 980 cm^{-1} , and 1082 cm^{-1} . This is in agreement with the observations in the Raman spectrum of KTiOAsO_4 , where main differences compared with KTP can be spotted in the $350\text{--}550\text{ cm}^{-1}$ regions and $>900\text{ cm}^{-1}$, while other spectral features are much less affected.^{38,47}

B. Visualization and analysis of domain structures

The realized visualization of domain structures by Raman spectroscopy in KTP is observed to be very similar to the behavior previously reported in the materials LN and

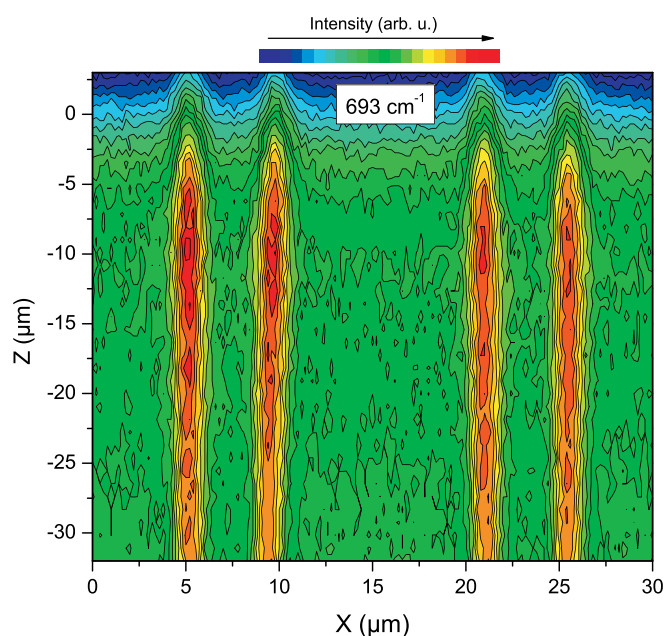


FIG. 6. Cross section of a domain structure along an xz -plane visualized based on the 693 cm^{-1} line. It should be noted that a periodic signal can also be detected for $z > 0$ due to limitations of optical resolution.

LT, where either the scattering efficiency of certain phonons is enhanced or decreased at DWs and phonon frequency shifts play only a minor role.^{10,11,25,27,51} Theory predicts a width of 180° ferroelectric DWs in the order of only a few unit cells for various ferroelectric materials,^{58–60} which have also been observed with high resolution TEM.^{61–63} While in this work, a typical DW FWHM of $\Delta x \approx 1.5\ \mu\text{m}$ is measured via confocal Raman microscopy as shown in Fig. 3. This is a typical length scale observed by the same method in LN and LT as well.^{10,51} The observed FWHM of the DW signature is independent of the used phonon. Whereby, the DW signatures appear significantly larger than the lateral resolution of the microscope, but also much larger than typical widths reported with PFM, where DWs in KTP appear to be $\Delta x \approx 20\text{--}80\text{ nm}$ wide.¹⁴ This is similar in LN and LT, where different techniques result in various values for the DW width.^{14,25,64,65} This behavior can be explained by the different contrast mechanisms of the respective techniques, which are sensitive for different physical properties. In particular, studies in LN with synchrotron X-rays have shown strain fields in LN, which can extend up to $50\ \mu\text{m}$ around DW.^{66,67} This strain is also suggested to be responsible for the contrast mechanism enabling the visualization of DWs by Raman spectroscopy. A theoretical model suggests that this strain leads to a change in polarizability via elasto-optic and electro-optic couplings, and hence leading to an intensity variation observed for certain phonon modes.⁶⁸ Further, the DW acts as an extended defect relaxing selection rules and thus leading to different scattering efficiencies.⁵⁸

A closer inspection of the phonon modes, which are sensitive to DWs, reveals that the phonons, which are most sensitive for DWs, are either related to K^+ ion displacements or internal modes of the TiO_6 octahedron (Table II). Both structures contribute to the inner polarization,^{3,36,37} which explains the sensitivity of these modes to changes in the inner polarization in the vicinity of DWs. The PO_4 tetrahedron is nearly symmetric and does not contribute

significantly to the polarization field. Therefore, the PO_4 vibrations show no strong connection to changes in the domain structures as observed in the spectra, as, for example, seen from the mode at 368 cm^{-1} or in the $>900\text{ cm}^{-1}$ region. This picture may also present a reason, why A_2 phonons are not sensitive to DWs. The A_2 branch is Raman active, but not IR active, which means that the displacement patterns of A_2 phonons are of non-polar character. Therefore, these modes do not couple to the inner polarization field. In LN and LT, a polarity contrast between as-grown and as-poled domains was observed, which vanishes after annealing.^{10,27} Here, also differences in transitions from z to $-z$ and $-z$ to z domains have been reported,^{10,68} which have been explained by the presence of residual surface charges after poling in LN and LT. These are unlikely in KTP due to the high ionic conductivity. Any charges would be quickly compensated by K^+ ions. This might explain, why no polarity contrast or depth dependence has been observed in KTP in this study so far.

V. CONCLUSION

Confocal Raman spectroscopy has been applied to study the vibrational properties of both, bulk and z-cut PPKTP. In this context, specific phonon modes are found to be sensitive for domain walls, which allows for high-contrast images of domain structures in KTP. The imaging procedure is found to be similar to other ferroelectrics and is explained by strain fields around domain walls, which modify the Raman scattering efficiency through electro-optic and elasto-optic couplings. Depth resolved analysis reveals no depth dependent behavior in KTP, which is in contrast to the observations in LN and LT. This is possibly due to the absence of surface charges in KTP due to the high ionic conductivity. The Raman bands, which show the strongest modification at DWs, are most likely either related to the K^+ ion or the TiO_6 tetrahedron, which both have been reported to have a strong connection to the ferroelectric polarization field. Hence, these modes show a strong coupling to strain and modification of electric fields in the vicinity of DWs. In the future, a more detailed understanding of the underlying mechanisms may be possible based on *ab-initio* calculations of Raman scattering efficiencies.⁶⁹ So far, we have applied our method only to z-cut domain structures. The Raman analysis can easily be extended to study x- and y-face domain structures, which cannot be visualized by selective etching in KTP.¹² Here, Raman imaging can be employed for a three-dimensional, noninvasive analysis of ferroelectric domain structures in KTP.

ACKNOWLEDGMENTS

The authors would like to acknowledge financial support by the Deutsche Forschungsgemeinschaft (DFG) via the SFB/TRR 142 and from the German Federal Ministry of Education and Research (BMBF) through Grant No. 16 KIS 0126 of the Q.com project.

¹J. D. Bierlein and C. B. Arweiler, *Appl. Phys. Lett.* **49**, 917 (1986).

²J. D. Bierlein and H. Vanherzeele, *J. Opt. Soc. Am. B* **6**, 622 (1989).

³N. I. Sorokina and V. I. Voronkova, *Crystallogr. Rep.* **52**, 80 (2007).

⁴M. E. Hagerman and K. R. Poeppelmeier, *Chem. Mater.* **7**, 602 (1995).

⁵G. Hansson, H. Karlsson, S. Wang, and F. Laurell, *Appl. Opt.* **39**, 5058 (2000).

⁶N. Argiolas, M. Bazzan, A. Bernadi, E. Cattaruzza, P. Mazzoldi, P. Schiavuta, C. Sada, and U. Hangen, *Mater. Sci. Eng., B* **118**, 150 (2005).

⁷M. C. Gupta, W. P. Risk, A. C. G. Nutt, and S. D. Lau, *Appl. Phys. Lett.* **63**, 1167 (1993).

⁸F. Laurell, M. G. Roelofs, W. Bindloss, H. Hsiung, A. Suna, and J. D. Bierlein, *J. Appl. Phys.* **71**, 4664 (1992).

⁹R. Hölscher, W. G. Schmidt, and S. Sanna, *J. Phys. Chem. C* **118**, 10213–10220 (2014).

¹⁰R. Hammoun, M. D. Fontana, P. Bourson, and V. Y. Shur, *Appl. Phys. A* **91**, 65 (2008).

¹¹V. Y. Shur, P. S. Zelenovskiy, M. S. Nebogatikov, D. O. Alikin, M. F. Sarmanova, A. V. Ievlev, E. A. Mingaliev, and D. K. Kuznetsov, *J. Appl. Phys.* **110**, 052013 (2011).

¹²C. Canalias, V. Pasiskevicius, A. Fragemann, and F. Laurell, *Appl. Phys. Lett.* **83**, 734 (2003).

¹³N. Ohnishi and T. Iizuka, *J. Appl. Phys.* **46**, 1063 (1975).

¹⁴J. Wittborn, C. Canalias, K. V. Rao, R. Clemens, H. Karlsson, and F. Laurell, *Appl. Phys. Lett.* **80**, 1622 (2002).

¹⁵J. Hellström, R. Clemens, V. Pasiskevicius, H. Karlsson, and F. Laurell, *J. Appl. Phys.* **90**, 1489 (2001).

¹⁶T. Kämpfe, P. Reichenbach, M. Schröder, A. Haußmann, L. M. Eng, T. Woike, and E. Soergel, *Phys. Rev. B* **89**, 035314 (2014).

¹⁷A. Fragemann, V. Pasiskevicius, and F. Laurell, *Appl. Phys. Lett.* **85**, 375 (2004).

¹⁸S. J. Holmgren, V. Pasiskevicius, S. Wang, and F. Laurell, *Opt. Lett.* **28**, 1555 (2003).

¹⁹S. Kurimura and Y. Uesu, *J. Appl. Phys.* **81**, 369 (1997).

²⁰S. I. Bozhevolya, J. M. Hvam, K. Pedersen, F. Laurell, H. Karlsson, T. Skettrup, and M. Belmonte, *Appl. Phys. Lett.* **73**, 1814 (1998).

²¹G. Berth, V. Wiedemeier, K. Hüsch, L. Gui, H. Hu, W. Sohler, and A. Zrenner, *Ferroelectrics* **389**, 132 (2009).

²²G. Berth, V. Quiring, W. Sohler, and A. Zrenner, *Ferroelectrics* **352**, 78 (2007).

²³D. Gardiner, H. Bowley, P. Graves, D. Gerrard, J. Loudon, and G. Turrell, in *Practical Raman Spectroscopy*, edited by D. J. Gardiner and P. R. Graves (Springer, Berlin, Heidelberg, 2012).

²⁴R. Loudon, *Adv. Phys.* **13**, 423 (1964).

²⁵P. Capek, G. Stone, V. Dierolf, C. Althouse, and V. Gopalan, *Phys. Status Solidi C* **4**, 830 (2007).

²⁶L. Mateos, L. E. Bausa, and M. O. Ramirez, *Opt. Mater. Express* **4**, 1077 (2014).

²⁷G. Berth, W. Hahn, V. Wiedemeier, A. Zrenner, S. Sanna, and W. G. Schmidt, *Ferroelectrics* **420**, 44 (2011).

²⁸M. Deluca, M. Higashino, and G. Pezzotti, *Appl. Phys. Lett.* **91**, 091906 (2007).

²⁹G. Pezzotti, M. Higashino, K. Tsuji, and W. Zhu, *J. Eur. Ceram. Soc.* **30**, 199 (2010).

³⁰G. Pezzotti, A. Matsutani, and W. Zhu, *J. Am. Ceram. Soc.* **93**, 256 (2010).

³¹I. P. Kaminow and W. D. Johnston, *Phys. Rev.* **160**, 519 (1967).

³²R. H. Lyddane, R. G. Sachs, and E. Teller, *Phys. Rev.* **59**, 673 (1941).

³³A. S. Chaves and S. P. S. Porto, *Solid State Commun.* **13**, 865 (1973).

³⁴A. Ridah, P. Bourson, M. D. Fontana, and G. Malovichko, *J. Phys.: Condens. Matter* **9**, 9687 (1997).

³⁵R. Mouras, M. D. Fontana, P. Bourson, and A. V. Postnikov, *J. Phys.: Condens. Matter* **12**, 5053 (2000).

³⁶M. Yashima and T. Komatsu, *Chem. Commun.* **2009**, 1070.

³⁷S. T. Norberg, P. A. Thomas, and M. G. Tucker, *J. Phys.: Condens. Matter* **23**, 175401 (2011).

³⁸G. Watson, *J. Raman Spectrosc.* **22**, 705 (1991).

³⁹S. Sanna, G. Berth, W. Hahn, A. Widhalm, A. Zrenner, and W. G. Schmidt, *Ferroelectrics* **419**, 1 (2011).

⁴⁰M. Jain, J. K. Lotsberg, J. J. Stamnes, and Ø. Frette, *Opt. Commun.* **266**, 438 (2006).

⁴¹D. Jiang and J. J. Stamnes, *Opt. Commun.* **174**, 321 (2000).

⁴²D. Jiang and J. J. Stamnes, *Opt. Commun.* **163**, 55 (1999).

⁴³M. J. Nasse and J. C. Woehl, *J. Opt. Soc. Am. A* **27**, 295 (2010).

⁴⁴H. Kianirad, A. Zukauskas, T. Frisk, C. Canalias, and F. Laurell, *Opt. Express* **23**, 636 (2015).

- ⁴⁵H. Karlsson, F. Laurell, and L. K. Cheng, *Appl. Phys. Lett.* **74**, 1519 (1999).
- ⁴⁶G. E. Kugel, F. Brèhat, B. Wyncke, M. D. Fontana, G. Marnier, C. Carabatos-Nedelec, and J. Mangin, *J. Phys. C: Solid State Phys.* **21**, 5565 (1988).
- ⁴⁷C. Tu, A. R. Guo, R. Tao, R. S. Katiyar, and R. Guo, *J. Appl. Phys.* **79**, 3235 (1996).
- ⁴⁸M. J. Bushiri, V. P. M. Pillai, R. Ratheesh, and V. U. Nayar, *J. Phys. Chem. Solids* **60**, 1983 (1999).
- ⁴⁹S. Röhrig, C. Krautgasser, R. Bermejo, J. L. Jones, P. Supancic, and M. Deluca, *J. Eur. Ceram. Soc.* **35**, 4321 (2015).
- ⁵⁰R. Ossikovski, Q. Nguyen, G. Picardi, J. Schreiber, and P. Morin, *J. Raman Spectrosc.* **39**, 661 (2008).
- ⁵¹P. S. Zelenovskiy, M. D. Fontana, V. Y. Shur, P. Bourson, and D. K. Kuznetsov, *Appl. Phys. A* **99**, 741 (2010).
- ⁵²P. Török, S. J. Hewlett, and P. Varga, *J. Microsc.* **188**, 158 (1997).
- ⁵³R. W. Boyd, *Nonlinear Optics* (Academic Press, 2003).
- ⁵⁴R. Menzel, *Photonics: Linear and Nonlinear Interactions of Laser Light and Matter* (Springer Science & Business Media, 2013).
- ⁵⁵R. Pisarev, R. Farhi, P. Moch, and V. Voronkova, *J. Phys.: Condens. Matter* **2**, 7555 (1990).
- ⁵⁶P. I. Tordjman, E. Masse, and J. C. Guitel, *Z. Kristallogr.* **139**, 103 (1974).
- ⁵⁷G. Herzberg, *Infrared and Raman Spectra of Polyatomic Molecules* (D. Van Nostrand, 1975).
- ⁵⁸V. Gopalan, V. Dierolf, and D. A. Scrymgeour, *Annu. Rev. Mater. Res.* **37**, 449 (2007).
- ⁵⁹J. Padilla, W. Zhong, and D. Vanderbilt, *Phys. Rev. B* **53**, R5969 (1996).
- ⁶⁰B. Meyer and D. Vanderbilt, *Phys. Rev. B* **65**, 104111 (2002).
- ⁶¹C. Jia, S. Mi, K. Urban, I. Vrejoiu, and M. Alexe, *Nat. Mater.* **7**, 57 (2008).
- ⁶²L. A. Bursill and P. J. Lin, *Ferroelectrics* **70**, 191 (1986).
- ⁶³Y. B. Chen, M. B. Katz, X. Q. Pan, R. R. Das, D. M. Kim, S. H. Baek, and C. B. Eom, *Appl. Phys. Lett.* **90**, 072907 (2007).
- ⁶⁴D. A. Scrymgeour and V. Gopalan, *Phys. Rev. B* **72**, 024103 (2005).
- ⁶⁵T. J. Yang, V. Gopalan, P. J. Swart, and U. Mohideen, *Phys. Rev. Lett.* **82**, 4106 (1999).
- ⁶⁶K. Hassani, M. Sutton, M. Holt, Y. Zuo, and D. Plant, *J. Appl. Phys.* **104**, 043515 (2008).
- ⁶⁷T. Jach, S. Kim, V. Gopalan, S. Durbin, and D. Bright, *Phys. Rev. B* **69**, 064113 (2004).
- ⁶⁸M. D. Fontana, R. Hammoum, P. Bourson, S. Margueron, and V. Y. Shur, *Ferroelectrics* **373**, 26 (2008).
- ⁶⁹S. Sanna, S. Neufeld, M. Rüsing, G. Berth, A. Zrenner, and W. G. Schmidt, *Phys. Rev. B* **91**, 224302 (2015).